Journal of Oceanography, Vol. 53, pp. 53 to 66. 1997

Wind Effects on Sub-Tidal Currents in Puget Sound

HIROSHI MATSUURA[1]* and GLENN A. CANNON[2]

[1]*School of Oceanography, University of Washington, Seattle, WA 98195, U.S.A.*
[2]*Pacific Marine Environmental Laboratory, National Oceanic and Atmospheric Administration, 7600 Sand Point Way N.E., Seattle, WA 98115, U.S.A.*

(Received 29 November 1995; in revised form 8 June 1996; accepted 14 June 1996)

Wind effects on sub-tidal currents are studied using current meter records obtained at six moorings across the main basin of Puget Sound. High correlations between wind speeds and currents are found near the surface and at mid-depths of about 100 m. Empirical Orthogonal Function analysis applied to the axial currents in 1984 and 1985 shows that mode 1, containing over 60% of the variance, is highly correlated with wind speed even without any near surface current records. When near surface stratification is strong, direct wind effects are limited to the upper 30 m with counter currents in the lower layer indicating a baroclinic response. The transport in the lower layer almost balances the transport in the upper layer. When near surface stratification is weak, direct wind effects on currents can be detected to about 100 m. In this case, there is no clear and consistent depth at which one can separate the upper from the lower layer. Time series show that the acceleration in the surface layer initially increases in the same direction as the wind when the wind starts blowing, but it reaches a maximum, starts decreasing, and eventually changes to the opposite direction (decelerates) while the wind continues to blow in one direction. Results of a continuously stratified normal mode model and estimations from the observations suggest that friction at solid boundaries is a major cause of these phenomena. The model shows that modal currents of normal modes 2 and 3 are as important as mode 1, although the resultant vertical structure of total current shows a two-layer type pattern with only one zero crossing. The effect of the baroclinic pressure gradient is only apparent at low frequencies and among lower modes.

Keywords:
· Wind effect,
· Normal mode model,
· Fjord circulation,
· EOF,
· Puget Sound.

1. Introduction

The mean circulation of many estuaries is described as a two layer flow with the surface water flowing out of the estuary and deep water flowing into the estuary. Deviations from this mean circulation due to wind effects have been studied by many authors both in shallow and deep estuaries. For example, in Chesapeake Bay, Pritchard and Vieira (1984) showed low-pass filtered currents were highly correlated with surface wind through the water column. The surface current was enhanced in the same direction as the wind and mid to bottom currents were in the opposite direction. Unlike shallow estuaries, fjords usually are characterized by deep channels. Using similarity methods, Hansen and Rattray (1965) and Winter (1973) showed that the wind effect on the steady-state fjord circulation was a decrease in the depth of the maximum return flow and an increase in the amplitude of the return flow as down-fjord wind stress increased. The observed wind effects on the surface layer in fjords have been described by, among others, Pickard and Rodgers (1959), Farmer and Osborn (1976) and Buckley and Pond (1976). Svendsen and Thompson (1978) made observations of currents in a Norwegian fjord not only at the surface but also at depths below the pycnocline.

Puget Sound is a fjord type estuary which is connected to the North Pacific Ocean through the Strait of Juan de Fuca (Fig. 1). The bottom is relatively flat, with depths of about 200 m, and it is bounded by sills both seaward (Admiralty Inlet, 65 m) and landward (Narrows, 45 m). The stratification in Puget Sound is strongly affected by annual variation of run-off and mixing over the sills as well as events such as storms on a much shorter time scale. Friebertshauser and Duxbury (1972) showed that the major runoff into Puget Sound is from Skagit River (the location of this river is outside of Fig. 1) through Possession Sound (northern end of the Puget Sound; Fig. 1) with the maxima in December and in June. The winter maximum is due to precipitation, and the maximum in early summer is due to snow melt. In

*Current Affiliation: JAMSTEC, 2-15, Natushima-cho, Yokosuka-shi, Kanagawa, 237, Japan.

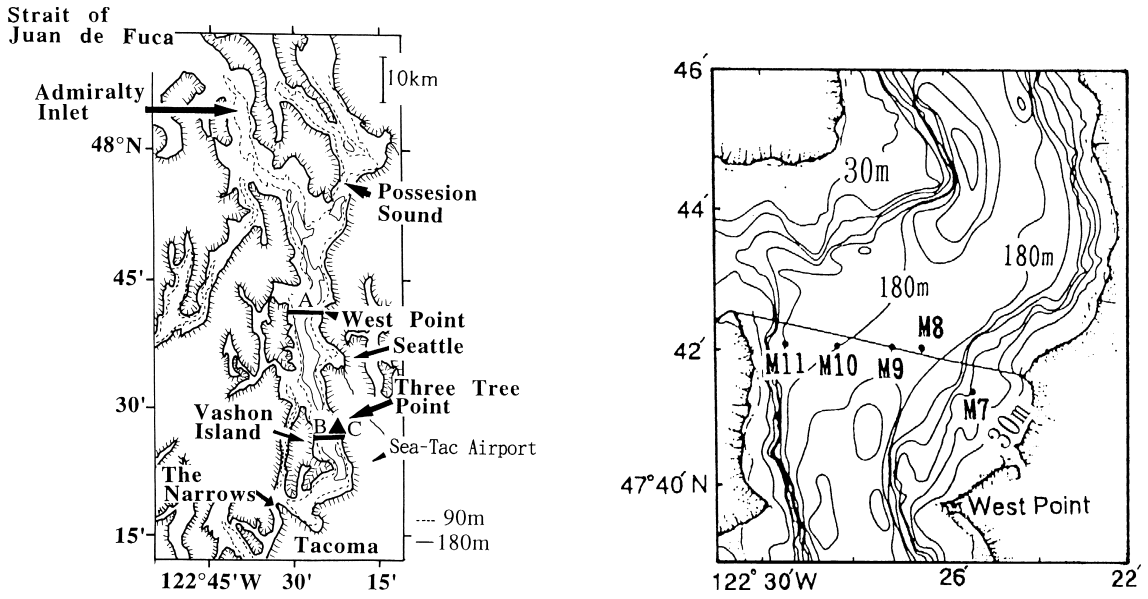

Fig. 1. Map of the mooring site (right panel; Line A, left panel) and of the surrounding area (left panel). Locations of moorings, except M6 which was very close to M9, are shown as solid dots. The solid triangle, C, is the location of the weather station. The contour interval of bottom topography in the right panel is 30 m.

general, temperature has little effect on vertical distribution of density when compared with salinity. Fresher water from runoff south of the Narrows appears to become mixed over the sill, whereas runoff in the area between the Narrows and Possession Sound is small. These factors produce relatively high salinity water near the surface in Puget Sound except near Possession Sound and relatively weak stratification compared with other fjords.

Previous studies in Puget Sound noted that wind has significant effects on sub-tidal circulation (Cannon, 1983; Bretschneider *et al*., 1985). Bretschneider *et al*. (1985; hereafter BA) used Empirical Orthogonal Function (EOF) analysis near Three Tree Point (Fig. 1, Line B) to point out that wind effects were the dominant mode and had strong influence at the surface and weak counter influence at mid-depths on the along-channel currents. In 1985, Pacific Marine Environmental Laboratory, National Oceanographic and Atmospheric Administration (PMEL/NOAA) conducted extensive current meter observations near West Point (Fig. 1, Line A) for about two months with CTD observations at the beginning and at the end of this period. Currents were observed at 6 moorings across the channel from near the surface to near the bottom (Fig. 1, Table 1).

The primary purpose of this paper is to describe observed wind effects on sub-tidal currents in Puget Sound and to explain the observed phenomena using a continuously stratified normal-mode model with linear friction and weak stratification. Matsuura (1995; hereafter MA) described an application of a two-layer model to the wind driven sub-tidal currents in Puget Sound with strong near-surface stratification. However, near surface stratification in Puget Sound is often too weak to justify use of the two-layer model.

2. Data

Data used in this paper were collected in 1984 and 1985, and locations of the moorings are shown in Fig. 1. The 1984 data had been used intensively to study bottom water intrusions including numerical modeling applications (Cannon *et al*., 1990; Lavelle *et al*., 1991). The results of analysis of these data are included in this paper to complement the 1985 data. These data consisted of two moorings; one had current meters at 30 and 50 m and the other had current meters at 100, 115, 135, 155, 165, 185 and 195 m excluding those which failed and the one which was not used. These moorings were located very close together near the mooring M9 (Fig. 1) and are treated as a single mooring in this paper. All current meters were Aanderaa RCM-4's, and the sampling interval was 30 minutes. The sampling period was from November, 1983 to April, 1984. The wind data were measured at Three Tree Point (Fig. 1, Solid triangle C) from January to September with a sampling interval of one hour. CTD records were from December, 1983, February, March, and April, 1984.

The 1985 data consisted of six moorings deployed to measure the cross-channel distribution of currents near West Point (Fig. 1, Line A). Moorings M6 and M9 were deployed close together (approximately 270 m apart) and are treated as a single mooring. ACM-2, Vector averaging current meters, were used at M6. All other current meters were RCM-4's with conductivity, temperature and pressure

sensors. Depths of current meters excluding those failed are noted in Table 1. An inter comparison between RCM-4 and ACM-2 meters was made by Pashinski (1985). A scatter diagram between axial currents with 2.85 hour filter measured by the ACM-2 at 4 m and the RCM-4 at 5 m at M6 (this current meter failed later and thus not included in Table 1) showed no systematic deviation depending on the amplitude of currents. These two records appeared to be linearly correlated with a correlation coefficient of 0.95 (number of data is 1981). In Puget Sound swell is rarely observed and wind waves do not fully develop due to limited fetch. These conditions may contribute to the differences seen in our data from other inter comparison experiments of current meters. Thus, we corrected data obtained by RCM-4 near the surface by multiplying a constant. Wind data were obtained at Three Tree Point. The 1985 data were from April to July for most of the records. The sampling interval of most of the current meter records was 30 minutes with a few at 20 minutes. The sampling interval of wind records was one hour. CTD records were obtained on March 18, April 10 to 12, April 16 and June 28. Salinity records obtained from RCM-4's were calibrated with the CTD records.

3. Observations

A 35-hours filter was used to remove high frequency and tidal components such as diurnal tide. After filtering, data were sub-sampled at 6-hour intervals. In some of the following analyses, a high-pass filter was applied to remove low-frequency components such as the fortnight tide. The combination of these two filters is noted as a band-pass filter. Wind stress was computed using the method of Large and Pond (1981) on unfiltered data with filters applied afterward. Statistical tests of EOF use "rule N" (Preisendoefer *et al.*, 1981). The confidence limits of statistical significance is 95%.

3.1 Stratification

Strong stratification tends to occur between 10 and 30 m in Puget Sound. Figure 2 shows the time series of salinity measured by RCM-4 at 5, 22, 44 and 153 m at M10 in 1985. Salinity deeper than 22 m shows a declining trend with short-time scale small perturbations while the salinity at 5 m has occasional large decreases. The short salinity drops at 5 m are synchronous with southward wind events, and they are probably caused by advection of fresher water pool from the northern end of the main basin near the entrance of Possession Sound. In the case of the salinity drop beginning April 30, the wind started blowing southward at 1200 on April 29 and the current at 5 m became southward at 0000 on April 30 (Fig. 4). The maximum salinity drop was at 0600 on May 2. An approximate estimate of the southward movement of water at 5 m using the current meter record at this depth is about 20 km between 1200, April 29 and 0600, May 2, a distance approximately from the entrance of Possession

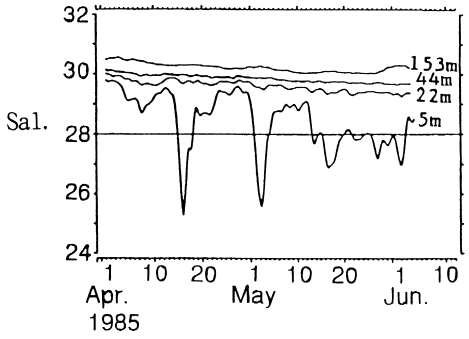

Fig. 2. Time series of salinity at 5 m, 22 m, 44 m and 153 m at M10 in 1985.

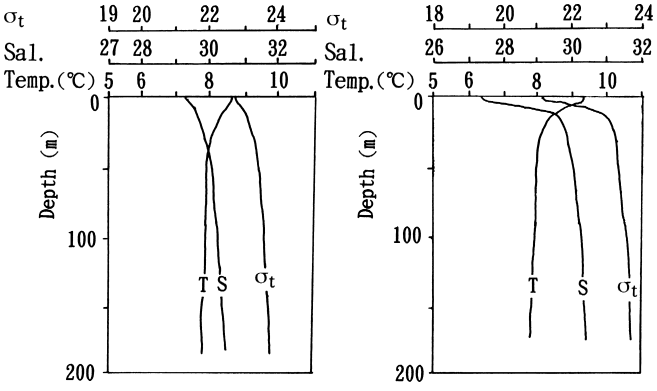

Fig. 3. Vertical distributions of temperature (*T*), salinity (*S*) and σ_t (σ_t) averaged over 36 CTD casts conducted between April 10–12 (left panel) and averaged over 5 CTD casts on April 16 (right panel) in 1985.

Sound to the mooring site (about 23 km). Another relatively large drop in salinity at 5 m continues for about a month beginning May 5. This is probably due to unusually large precipitation at that time.

The left panel of Fig. 3 shows the result of the average of 36 CTD casts near the mooring from April 10–12, 1985 when the salinity difference between 5 and 22 m is relatively small (Fig. 2). Relatively large density changes occurred in the upper 20 m, and small density changes can be seen below 20 m. Compared with CTD records in 1984, however, the stratification near the surface was stronger in 1985. The right panel of Fig. 3 shows the result of an average of 5 CTD casts near the mooring on April 16, 1985. Figure 2 shows that this is the peak of the large decrease of salinity at 5 m.

3.2 Wind and current

Winds at Sea-Tac airport and at West Point were highly correlated to winds at Three Tree Point, and wind record at Three Tree Point is used throughout this paper. Wind is

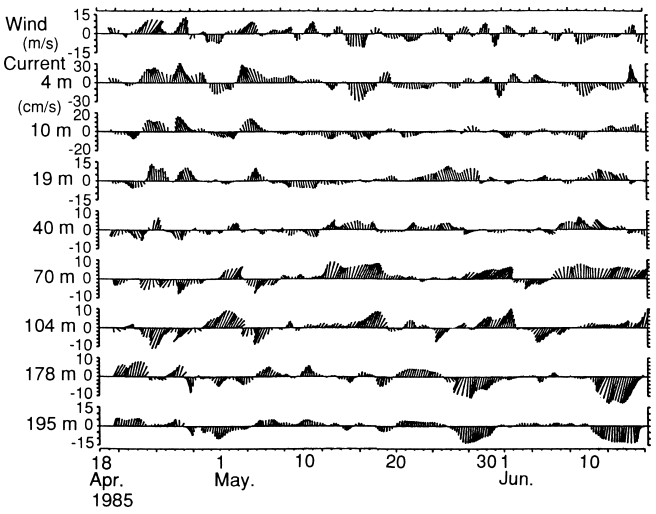

Fig. 4. Vector plots of wind speed and currents at M9. Time averages of each record are removed.

strongly aligned to the channel direction. Power spectra of axial winds show a prominent peak at 1 cycle per day (cpd) which is a land-sea breeze and a broad peak around 0.3 cpd which is a local synoptic scale. The wind field in this region has been discussed in detail by Cokelet (1992).

Time averaged currents are northward from the surface to about 50 m and southward from there to the bottom. Figure 4 shows time series of currents at M6 and M9 and wind speed after subtracting the time averages. Current at 4 m is strongly affected by wind. A high correlation between wind and current is noticeable at 10 m until about May 6, 1985. Afterwards the deviation from wind becomes larger. This change is more obvious at 19 m. Currents at 178 and 195 m are highly correlated with each other and show occasional strong southward flow (May 1 and 28 and June 13). These are accompanied with salinity increases and are considered to be deep-water intrusions (Cannon *et al.*, 1990).

4. Data Analysis

Table 1 shows correlation coefficients between axial currents and wind speed in 1984 and 1985. In 1984 the negative correlations were grater than the 95% confidence limits below 100 m with the maximum at about 135 m. The time lag for maximum correlation is 18 ± 3 hours. In 1985, high correlations are seen near the surface with a time lag of 6 ± 3 to 12 ± 3 hours, but at 20 m, the correlations are not statistically significant. At 100 m, the correlations are negative and statistically significant, and the time lags for the maximum also are 12 ± 3 hours. Thus, the deep negative correlation of currents with wind speed is a significant and persistent feature.

The cross-sectional distribution of the axial currents with northward wind is shown in Fig. 5(a) and with southward wind in Fig. 5(b) in 1985. The time averages of individual records have been subtracted. When winds are northward, the currents in both the surface and mid-depth layers are increased, but in opposite directions. The subsurface response is centered at approximately the middle of the channel, and forms a distinctive core at about 120 m. When winds are southward, the response is similar but opposite in sign. The zero crossing for both cases is at about 50 m; however this appears to be affected by stratification. Table 1 and Fig. 5 clearly show current responses to wind forcing at the surface and counter responses at mid-depths around 100 m.

EOF analysis applied to the 1984 axial currents shows that 60% of the total variance contributes to mode 1 and is statistically significant. A band-pass filter (0.1–0.7 cpd) was applied to eliminate the effect of the fortnight tidal component as well as of the high frequency tidal components prior to the computation. Figure 6(a) shows the time series of EOF mode 1 and axial wind speed after multiplying by an arbitrary constant to make comparison easier. Note that the there are no near surface current measurements in 1984. Figure 6(b) shows that the coherence between axial wind speed and EOF mode 1 has statistically significant peaks at 0.24 and 0.4 cpd. These frequencies are the same as where the wind has large energy. Figure 6(c) shows the vertical distribution of percent of variance contributed to this mode. The vertical distribution of eigenvectors (Fig. 6(d)) shows zero crossing between 30 m and 50 m and a local maximum at 155 m.

EOF analysis is also applied to the band pass filtered axial currents measured in 1985. Figure 7(a) shows time series of EOF mode 1 and axial wind speed after multiplying by an arbitrary constant. Figure 7(b) shows that the coherence between EOF mode 1 and axial wind speed is high, especially at frequencies with large wind energy. These figures indicate statistically that this is the component which is affected by wind. Mode 1 contains 69% of the total variance and is statistically significant. At the depths less than 10 m, over 90% of the variance contributes to this mode, and at 100 m, over 30% (Fig. 7(c)). The distribution of the eigenvectors shows a maximum at the surface and in the middle of channel at about 100 m (Fig. 7(d)). A distinctive core is seen in the lower layer.

The results of EOF analysis applied to all the data presented here, as well as the results of BA, show that the wind effects are represented by the lowest modes and have dominant effects on sub-tidal currents. The effects are strongest at the surface, but there is a local maximum at the mid-depths around 100 m in the opposite direction. In 1985, EOF mode 1 is expected to be heavily affected by data near the surface, because they are highly correlated each other and near surface currents are energetic. However, in 1984, wind effects also are the dominant mode even without any near-surface data. This has been confirmed by re-computing 1985's EOF without any data shallower than 20 m. EOF

Table 1. The correlation coefficients between wind speed and currents.

Table 1(a)

Depth (m)	Axis (degree)	Corr. A	Corr. B	Lag (hour)	95%
30	41	0.06	–0.46	66	0.29
50	54	–0.44	–0.45	6	0.40
100	62	–0.52	–0.55	12	0.44
115	57	–0.57	–0.62	12	0.44
135	50	–0.61	–0.68	18	0.40
155	51	–0.55	–0.65	18	0.40
165	57	–0.48	–0.57	18	0.41
185	48	–0.37	–0.46	18	0.42
195	40	–0.31	—	18	0.43

Table 1(b)

Mooring	Depth (m)	Axis (degree)	Corr. A	Corr. B	Lag (hour)	95%
M7	26	23	0.03	—	18	0.22
	47	32	–0.13	—	48	0.23
	76	25	–0.14	—	6	0.26
M8	22	32	0.15	0.15	36	0.14
	69	57	–0.22	—	12	0.27
	106	55	–0.24	–0.29	12	0.24
	152	47	–0.36	–0.42	12	0.24
	185	39	–0.25	–0.26	6	0.24
M6	4	28	0.67	0.80	12	0.33
	10	21	0.37	0.48	12	0.26
M9	19	27	0.13	—	24	0.28
	40	32	–0.20	—	12	0.25
	70	61	–0.17	—	12	0.31
	104	65	–0.31	–0.36	12	0.29
	178	50	–0.10	—	12	0.30
	195	40	–0.04	—	42	0.28
M10	5	22	0.74	0.79	6	0.30
	22	18	0.14	—	48	0.27
	44	22	–0.11	—	48	0.24
	73	73	–0.13	—	12	0.21
	111	90	–0.26	–0.35	12	0.20
	153	54	–0.22	–0.27	12	0.26
	179	34	–0.11	—	12	0.22
M11	19	7	0.14	–0.33	90	0.25
	41	2	0.13	—	84	0.21
	71	19	–0.08	0.25	48	0.21
	158	11	–0.09	0.35	42	0.19

Principle axes of currents are selected by directions of maximum variance and shown in column “Axis”. The direction of the wind is 0°T. Linear correlation coefficients are shown in column “Corr. A”. Maximum lagged linear correlation coefficients are shown in column “Corr. B”, and “—” in this column indicates maximum correlation is below the 95% confidence limit. Lags for the maximum correlation are shown in column “Lag”. 95% confidence limits are shown in column “95% limit”. In these estimation of confidence limits, time scales (Davis, 1976) are taken into consideration. Table 1(a) shows results of 1984 data and Table 1(b) shows results of 1985 data.

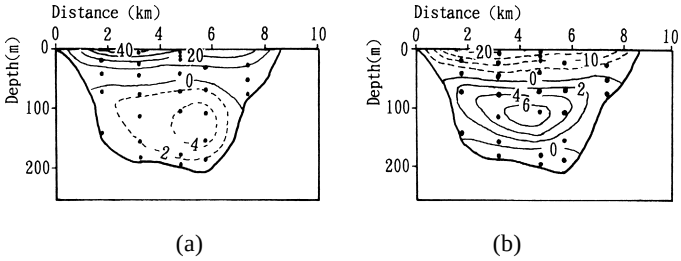

Fig. 5. Cross sectional distribution of axial currents at 1200, May 4, 1985, when winds were northward (left panel), and at 0600, May 1, 1985, when winds were southward (right panel). The average currents are subtracted. The solid contour lines (contour interval is 10 cm s^{-1} in the left panel and 2 cm s^{-1} in the right panel) show positive values (northward flow) and dashed contour lines (contour interval is 2 cm s^{-1} in the left panel and 2 cm s^{-1} in the right panel) show negative values. The solid dots show the locations of current meters.

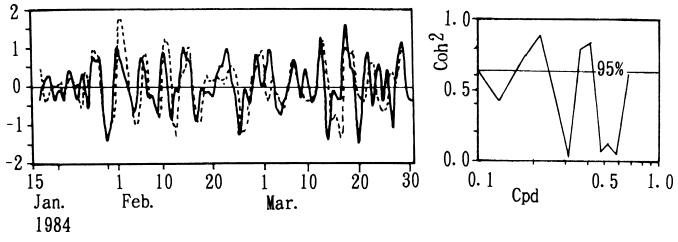

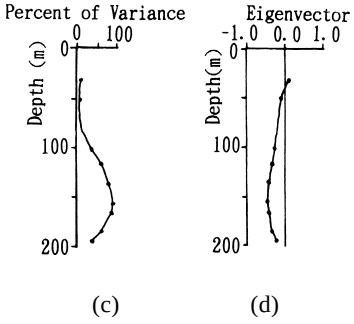

Fig. 6. (a) Time series of EOF mode 1 (dash line) of axial currents and axial wind speed multiplied by an arbitrary constant (solid line) of 1984. A band-pass filter (0.1–0.7 cpd) was applied. (b) Coherence between EOF mode 1 and wind speed. (c) Vertical distribution of percent of variance that contributes to EOF mode 1. (d) Vertical distribution of eigenvector of EOF mode 1.

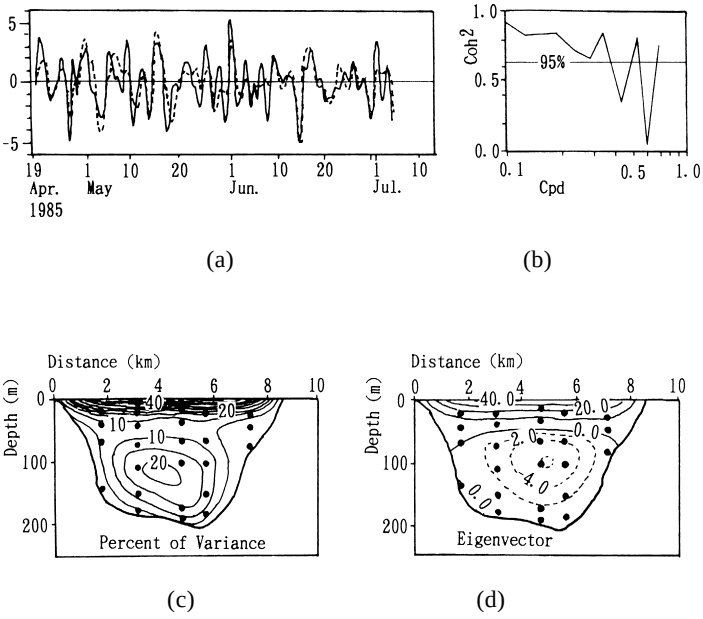

Fig. 7. (a) Time series of EOF mode 1 (dash line) of axial currents and axial wind speed (solid line; multiplied by an arbitrary constant) of 1985. Band pass filter (0.1–0.7 cpd) is applied. (b) Coherence between EOF mode 1 and wind speed. (c) Cross channel distribution of percent of variance which contributes to EOF mode 1. Contour interval is 5% and the solid dots show the locations of current meters. (d) Cross channel distribution of eigenvector of EOF mode 1. Solid contour lines with contour interval of 10 show positive values and dashed contour lines with contour interval of 2 show negative values.

mode 2 computed from both 1984 and 1985 do not correlate with wind. Although we did not try any further analysis of EOF mode 2, BA has shown that EOF mode 2 was correlated with bottom water intrusion near the Three Tree Point (Fig. 1, Line B).

Cross channel averaging was applied to 1985 data by using Akima's spline (IMSL) with the boundary conditions that velocity or acceleration is zero at the bottom and at the side boundary. To remove fortnight tidal component, a band pass filter (0.1–0.7 cpd) was applied prior to cross channel averaging. Figure 8 shows the examples of the time series of the vertical distribution of the cross channel averaged acceleration for the case (a) when stratification is strong and (b) when stratification is weak. Note that the scale of acceleration for (a) and (b) is different. When stratification is strong (Fig. 8(a)), response of current acceleration to wind near the surface appears to be limited to about 30 m. Figure 2 shows that a relatively large salinity difference between 5 m and 22 m persists for about a month from April 29. The time series of transports averaged across the channel from the surface to 30 m and from 30 m to the bottom show that transports in the upper and lower layer almost balance each

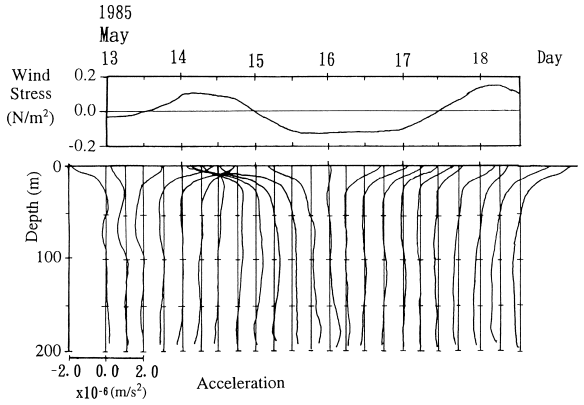

(a)

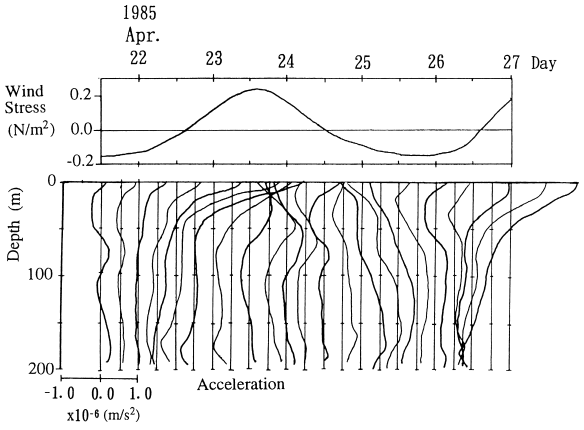

(b)

Fig. 8. (a) Time series of wind stress (upper panel) and the vertical distribution of cross channel averaged acceleration (lower panel) when stratification was strong. A band-pass filter (0.1–0.7 cpd) was applied to both, and the time interval of the lower panel is 6 hours. (b) Same as (a) when stratification was weak. Note that the scale of acceleration is different from (a).

other from about April 30 (Fig. 3, MA). This result indicates the variation of the transport is very strongly baroclinic and, thus, a two layer model was applied in MA for this period. Here, the term "barotropic" refers to the characteristic which is uniform in depth. However, during the earlier part of the 1985 observation period, the mismatch of the amplitudes of the transports between above and below 30 m is considerably larger than for the latter part of the 1985 observation period. Figure 8(b) shows that momentum exerted by the wind at the surface can propagate to about 100 m. Thus this mismatch probably is caused by the fact that the interface depth of 30 m is not appropriate during this period, rather it is caused by a stronger barotropic response.

5. Discussion

Figure 8(b) shows that accelerations near the surface start decreasing at 0600 and then, reverse sign at 1800 on April 23 while wind continues to blow northward. However, at 1800, accelerations at depths deeper than about 20 m are still positive. To understand the mechanism which causes the reversal of sign of acceleration while wind is kept blowing in one direction when stratification is weak, it is useful to have a corresponding cross channel averaged equation of motion,

$$\frac{\partial u}{\partial t} = -g\frac{\partial \eta}{\partial x} - \frac{g}{\rho_0}\int_z^{\eta}\frac{\partial \rho_1}{\partial x}dz_0 - \frac{\tau_{ss}}{\rho_0 W} + \frac{1}{\rho_0}\frac{\partial \mu}{\partial z} \qquad (1)$$

where u is the along channel velocity, t the time, x the along channel direction, g the gravitation constant, η the surface height, ρ_0 the averaged density, ρ_1 the perturbation part of density, τ_{ss} the stress at bottom (note that "bottom" exists at any depths due to the fact that side boundaries are not vertical wall), W the channel width and μ is the vertical component of the stress. In this equation, u, η, ρ_1 and μ are cross channel averaged. The advection terms are ignored since scale analysis shows they are at least one order smaller than the terms left in (1).

The first term of the right hand side of (1) is the barotropic pressure gradient due to the surface slope. Wind forcing may change the surface slope by generating barotropic and baroclinic motions. In general, for a semi-enclosed basin such as the main basin of Puget Sound, the speed of the surface set up due to the barotropic motion for wind forcing can be estimated from the channel length, 70 km, and the surface wave speed, 44 m s^{-1} (for bottom depth of 200 m). These values give about 26 minutes for the surface set up time which is much too short to explain the observed phenomena of decreasing and reversing of the sign of the acceleration while the wind blows in same direction. The set up speed of the surface slope due to the baroclinic motions can be 1 day if the propagation speed is 0.4 m s^{-1}, the evaluation of which is done using Csanady's method (Csanady, 1972). The time scale of the baroclinic set up is comparable to that of the observed phenomena. However, if this phenomenon is caused by the barotropic term, then its effect should be the same regardless of the depth. However, Fig. 8(b) shows that vertical distribution of the difference of the acceleration between 0000 and 1800 is not constant in depth. Therefore, the first term can not be a sole cause of this phenomena although it may be partially responsible through its contribution to the baroclinic motions.

The time difference of the acceleration at 5 m between 0000–1800, April 23 is 2.4×10^{-6} m s^{-2}. To achieve this difference, there should be a change of density gradient of 0.26 kg m^{-3} per km if the second term of the right hand side of (1) is responsible. From the CTD measurements conducted on April 10, the density at 5 m and above is relatively

uniform and does not show a difference of this magnitude. Since the wind during this event is northward, fresh water from the Skagit River is kept at the northern end of the basin, and an advection of fresher water to the mooring site is not expected (Fig. 2).

The estimation of amplitude of the stress terms, the third and the fourth terms in the right hand side of (1) is done with the domain of finite thickness between the depth of 5 and 10 m. In this case, these terms can be transformed into the stress normal to the boundaries and integrated along the boundaries. Using a quadratic law, data at M9 and M10, a drag coefficient $Cd = 3 \times 10^{-3}$ and assuming the length of the bottom at the depth between 5 m and 10 m is 100 m (Fig. 1), the time difference of cross channel averaged stress at sloping bottom between 0000-1800 April 23 is 3.4×10^{-6} m s^{-2} while the difference of the cross channel acceleration is 1.1×10^{-5} m s^{-2}. The time difference of the stress other than at the sloping bottom is 2×10^{-6} m s^{-2} from the vertical gradient of cross channel averaged velocities at these depths with an eddy viscosity of 1×10^{-2} $m^2 s^{-1}$. Adding these two, the amplitude of the variation of the stress term is slightly over half of that of the acceleration. This analysis indicates that the stress including those at the sloping side boundaries is probably responsible for the observed phenomena of decreasing and reversing of the sign of the acceleration while the wind blows in same direction since all other terms are, at least, order of magnitude smaller.

MA showed that the reversal of the acceleration was due to the friction by using a two-layer model when stratification was strong. He also showed that the current reversal (Buckley and Pond, 1976) may occur due to the baroclinic set up but that occurs much later than the reversal of acceleration. To further analyze this with weak stratification as in Fig. 8(b), a continuously stratified normal mode model is developed and applied. The model geometry and boundary conditions used in this paper are the same as those originally used by Farmer (1976) and then by MA. The channel is infinitely long with one end at $x = 0$. Wind is uniformly applied from the head at $x = 0$ to the mouth at $x = d = 70$ km (an approximate distance between the Narrows and the Admiralty Inlet). The bottom is flat at 200 m, and no sill exists at the mouth. Both velocity (u) and vertical perturbation (ζ) are continuous at $x = d$. Computations in the following sections were made at $x = 31.5$ km which is the approximate position of Line A (Fig. 1) where observations were made. Only the baroclinic modes are considered, and data are band pass filtered (0.1–0.7 cpd) unless otherwise mentioned.

5.1 Model

The set of the equations and derivation for a continuously stratified normal mode model can be found elsewhere (e.g., Gill, 1982), and therefore, the derivations are not presented here. The velocity, u, and vertical displacement ζ, which is defined by $\partial\zeta/\partial t \equiv -w$ (negative sign is added to have resultant equations same forms as those for a two-layer model), where w is the vertical velocity, are expanded in series,

$$u = \sum_{n=0}^{\infty} u_n(x,t)\frac{dQ_n(z)}{dz}, \tag{2}$$

$$\zeta = \sum_{n=0}^{\infty} \zeta_n(x,t)Q_n(z). \tag{3}$$

Cross-channel averaged equations of motion and continuity for mode n are

$$\frac{\partial u_n}{\partial t} = C_n^2 \frac{\partial \zeta_n}{\partial x} - r u_n + \phi_n, \tag{4}$$

$$\frac{\partial u_n}{\partial x} = \frac{\partial \zeta_n}{\partial t}, \tag{5}$$

$$\phi_n \equiv \int_{-H}^{0} \left\{ \frac{\partial \mu}{\partial z}\frac{dQ_n}{dz} \right\} dz \Big/ \int_{-H}^{0} \rho \left(\frac{dQ_n}{dz} \right)^2 dz \tag{6}$$

where t is the time, x the along channel direction positive outward with origin located at the head, z the vertical direction positive upward, C_n the n-th mode eigenvalue of the equation described below, r the friction coefficient (constant), $Q_n(z)$ the n-th vertical mode described below, H the bottom depth and μ the vertical stress which is $\mu = \rho K_z \partial u/\partial z$ with vertical eddy viscosity K_z and density ρ.

From this set of equations, the vertical mode, $Q_n(z)$, satisfies the following relations.

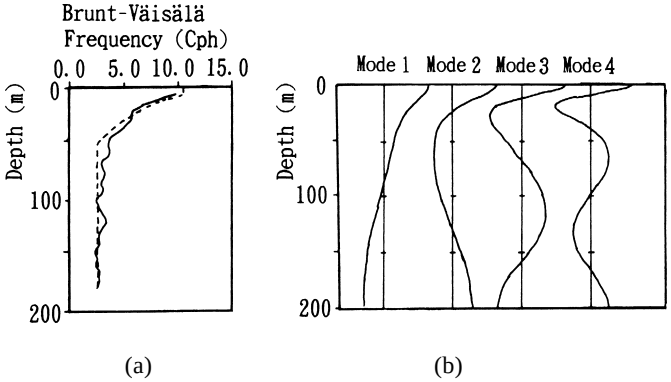

Fig. 9. (a) Vertical distributions of observed (solid line) and approximated (dashed line) Brunt Väisälä frequency for the earlier part of 1985. (b) Vertical distributions of dQ/dz of mode 1 through mode 4.

$$\frac{d^2Q_n}{\partial z^2} - \frac{N^2}{g}\frac{dQ_n}{\partial z} + \frac{N^2}{C_n^2}Q_n = 0, \tag{7}$$

$$\frac{dQ_n}{\partial z} + \frac{g}{C_n^2}Q_n = 0 \quad \text{at} \quad z = \eta, \tag{8}$$

$$Q_n = 0 \quad \text{at} \quad z = -H \tag{9}$$

where N is the Brunt Väisälä frequency. The eigenvalue problem described by (7)–(9) were solved by the method described by Csanady (1972) after ignoring the second term of (7) since the second term is $O(10^{-3}) \sim O(10^{-4})$ smaller than other terms after substituting typical values in the equation. In the case of Puget Sound, the vertical distribution of N appears to be approximated by a constant, a linear or an exponential function, or combinations of these. For the earlier part of the 1985 observations, the vertical distribution of N can be approximated by a constant between 0 and 6 m, an exponential decrease between 6 and 50 m, and a constant below 50 m. Figure 9(a) shows the vertical distribution of the modeled Brunt Väisälä frequency (dashed line) as well as the observed Brunt Väisälä frequency (solid line) averaged over 36 CTD casts between April 10 and 12 in 1985 (Fig. 3, Left panel). Figure 9(b) shows the vertical distribution of several modes of dQ_n/dz obtained from this method.

The stress function, ϕ_n, defined by (6), includes surface stress and internal stress. In the two-layer model, the first part is treated as a forcing function and the second part is included in the friction term as an interfacial stress. When eddy viscosity has the specific form,

$$K_z = K / N^2(z) \tag{10}$$

where K is a constant, the stress function can be separated into modes (Fjeldstad, 1963; McCreary, 1981) as

$$\phi_n = T_n - \frac{K}{C_n^2}u_n, \tag{11}$$

$$T_n \equiv Ts \Big/ \int_{-H}^{0} \rho\left(\frac{dQ_n}{dz}\right)^2 dz \tag{12}$$

where Ts is the surface stress and a function of time between $x = 0$ and $x = d$, but zero for $x > d$. dQ_n/dz are normalized by $dQ_n/dz = 1$ at $z = 0$. The bottom stress is assumed to be zero. (Note that friction coefficient r is included in this model and this represents friction at solid surfaces; i.e., at bottom and at side boundaries.) Substituting (11) into (4) yields,

$$\frac{\partial u_n}{\partial t} = C_n^2\frac{\partial \zeta_n}{\partial x} + T_n - \alpha_n u_n \tag{13}$$

where α_n, the effective friction coefficient, is defined by

$$\alpha_n \equiv r + \frac{K}{C_n^2}. \tag{14}$$

The amplitudes of these effective friction coefficients increase as the mode number increases because the phase speeds, C_n, decrease.

This shows that equation of motion of n-th mode, (13), and continuity, (5), have the same forms as those of the two-layer model (MA). Since both boundary/matching conditions and initial condition are the same as those of the two-layer model, the solution is, using the result of MA,

$$u_n = \int_0^t \left(C_n^2\frac{\partial \zeta_n(x,\sigma)}{\partial x} + T_n(\sigma)\right)e^{-\alpha_n(t-\sigma)}d\sigma \tag{15}$$

where $\partial\zeta_n(x,t)/\partial x$ is,

$$\begin{aligned}\frac{\partial \zeta_n}{\partial x} = \frac{1}{C_n}\int_0^t \Bigg[& T_n(t-\sigma)e^{-\frac{\alpha_n\sigma}{2}}\Bigg\{-\frac{\alpha_n x}{2C_n^2}\left(\sigma^2 - \frac{x^2}{C_n^2}\right)^{-1/2} I_1\left[\frac{\alpha_n}{2}\left(\sigma^2 - \frac{x^2}{C_n^2}\right)^{1/2}\right]H\left(\sigma - \frac{x}{C_n}\right) \\ & + \frac{\alpha_n(x+d)}{4C_n^2}\left(\sigma^2 - \frac{(x+d)^2}{C_n^2}\right)^{-1/2} I_1\left[\frac{\alpha_n}{2}\left(\sigma^2 - \frac{(x+d)^2}{C_n^2}\right)^{1/2}\right]H\left(\sigma - \frac{x+d}{C_n}\right) \\ & - \frac{\alpha_n(d-x)}{4C_n^2}\left(\sigma^2 - \frac{(d-x)^2}{C_n^2}\right)^{-1/2} I_1\left[\frac{\alpha_n}{2}\left(\sigma^2 - \frac{(d-x)^2}{C_n^2}\right)^{1/2}\right]H\left(\sigma - \frac{d-x}{C}\right)\Bigg\}\Bigg]d\sigma \\ & + \frac{1}{C_n^2}\left\{-T_n\left(t - \frac{x}{C_n}\right)e^{-\frac{\alpha_n x}{2C_n}} + \frac{1}{2}T_n\left(t - \frac{x+d}{C_n}\right)e^{-\frac{\alpha_n(x+d)}{2C_n}} - \frac{1}{2}T_n\left(t - \frac{d-x}{C_n}\right)e^{-\frac{\alpha_n(d-x)}{2C_n}}\right\}\end{aligned} \tag{16}$$

where I_1 is the modified Bessel function of order of 1 and H is the Heaviside function. Equation (16) shows that events due to wind forcing on baroclinic pressure gradient propagate from the boundaries with the speed C_n. Terms in (16) are separated into two groups; the one with modified Bessel function of the first order (the first three terms) and one without Bessel function. The latter group represents the effects of wind forcing which occurred at a time D/C_n before the present. Here D is the total distance between the position x and a boundary. These terms are rather simple functions if they are multiplied by C_n^2 as in the equation of motion, (13). Note that their amplitude decrease as C_n decreases, the distance between the position x and the boundaries increases or the eddy viscosity increases. The first group represents the cumulative effects of wind forcing at boundaries from $t = 0$ till D/C_n before the present (thus integration).

5.2 Comparison between observations and results of model

Once C_n and Q_n are determined, u_n are computed using (15) and (16). Then velocities at specified depths are computed using (2) up to the 15th mode. Integration of (15) is done numerically with variable intervals (shorter intervals for the higher modes) to avoid excessive computational time while maintaining accuracy. A standard case, $K = 3.4 \times 10^{-6}$ m^2/s^3 and $r = 2 \times 10^{-5}$/s, is chosen after comparing results from several computations in term of variance computed between April 23 and 29 with the observations, and to test the sensitivity to K, computations are made using 1.4×10^{-5} and 8.5×10^{-7} m^2/s^3.

Figure 10 shows the time series of the wind stress, observed cross channel averaged velocities and the velocities computed with this model with a standard value of K at several depths where measurements are typically made. The vertical lines in this figure show the dates when stratification changed significantly (Fig. 2). The model velocities at 5 and 10 m are larger than the observed velocities during the period when stratification is weak. After this period, observed velocities are larger than model velocities. This is expected because momentum input by wind would be confined in shallow surface layer due to the strong stratification. At a depth of 30 m, the model velocity agrees with the observations. At 50 m, the observed velocity is larger than the model velocity. At this depth, the observed current appears to be more highly correlated with the currents near the surface than with the currents at mid-depth (100 m). As the depth increases further, the agreement between model and observations improves. When the eddy viscosity is about 4 times larger, the agreement between the model and observations near the surface becomes better than in the standard case. However, the agreement between model and observations at all other depths becomes worse. When the eddy viscosity is about 4 times smaller, the amplitudes of the model velocities are larger than in the standard case at all depths. In this case, the model velocity at 50 m is apparently more highly correlated with the model velocities at greater depths.

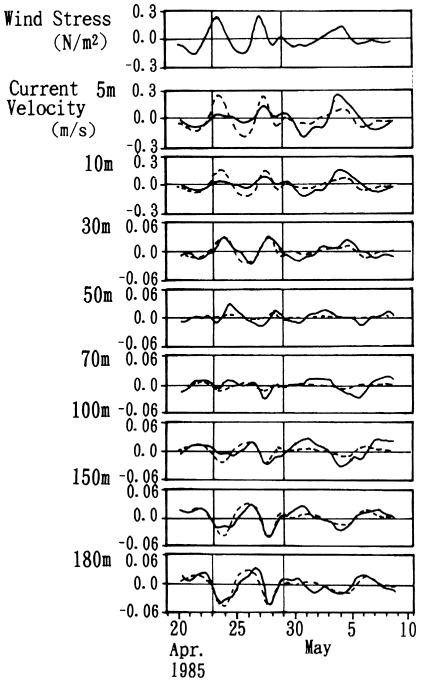

Fig. 10. Time series of cross channel averaged velocities (solid line) and model velocities (dashed line) at several depths. Top panel shows wind stress.

An alternative method for comparing results of the model with observations is to apply EOF analysis to both and compare the results. EOF computation applied to the observations is used as a filter to remove components not related to the wind forcing. For the sake of consistency, EOF is also applied to the model current to compare model result with observation since EOF's of the model results need not be connected in any way with the dynamical normal mode. As shown in the Appendix, dynamical normal modes are highly correlated each other but they are not identical. In the following text, EOF modes are referred as numbers added immediately after EOF such as EOF 1 to avoid confusion between EOF modes and normal modes.

Figure 11(a) shows time series of the EOF 1 of observed data and model results. To compute the EOF of the observed data, first, the cross-channel averaged velocities are computed at 5, 10, 30, 50, 100, 150, and 180 m and then, the EOF analysis is applied to these time series between April 23 and 29. To compute the EOF of the model results, velocities at these same depths are computed, and then the EOF is calculated. These procedures are taken to make the conditions of the two data sets as close as possible. The determination of these depths are based on the depths of the current meters (Table 1). The time series in Fig. 11(a) are multiplied by the value of the corresponding eigenvector at 150 m (Fig.

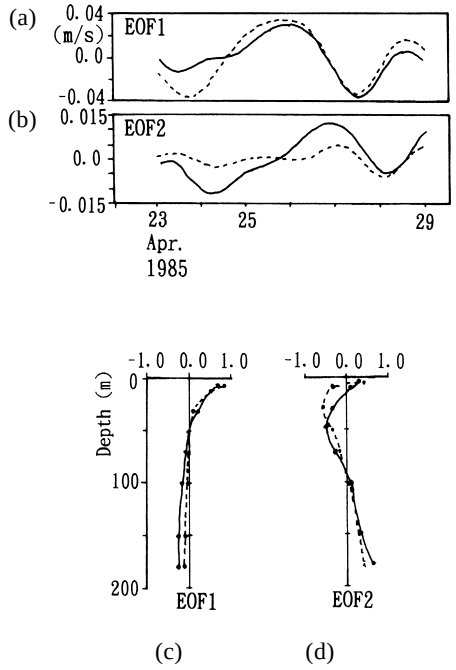

Fig. 11. Time series of EOF 1 (a) and of EOF 2 (b) of the cross channel averaged velocities (solid line) and the model velocities (dashed line). They are multiplied by the eigenvectors at 150 m to get m/s. The vertical distributions of eigenvector EOF 1 (c) and EOF 2 (d) of cross-channel averaged velocities (solid line) and of model velocities (dashed line).

11(c)) and, thus, unit is noted. Figure 11(b) shows time series of the EOF 2. The variation of EOF 2 lags behind the variation of EOF 1. The eigenvalue of EOF 1 of the observed data is 86.3 and of EOF 2 is 10.4. The eigenvalue of EOF 1 of the model is 99.7 and of EOF 2 is 0.3. These eigenvalues express the percent of variance accounted for by these modes. Applying the "rule N" (Preisendoefer *et al.*, 1981), EOF 1 is statistically significant but EOF 2 is not for both cases. Theoretically, model results do not contain any signal that is not caused by wind forcing. However, that is not true for observations. Therefore, although it appears that the EOF 2 of observation and model agree, it should be interpreted with a caution. The contamination of EOF 1 by EOF 2 is statistically insignificant for both cases (North *et al.*, 1982). Figure 11(c) shows the vertical distribution of the eigenvector of EOF 1. Amplitudes of EOF 1 of model results and of observations agree except near the surface (shallower than about 30 m) where the model result is approximately twice as large as observations. There is only one zero crossing and the depth of the zero crossing is shallower than the zero crossing of dynamical normal mode 1 (Fig. 9(b)). This is caused by the effect of the dynamical normal mode 2 and the higher dynamical normal modes. The magnitude of the eigenvalue of EOF 1 of the model velocities and the amplitudes of dynamical normal modal currents also supports that EOF 1 is not the result of one dynamical normal mode, but rather it is the mixture of many dynamical normal modes. The implication here is that, although statistical analysis such as EOF shows a pattern similar to the single mode response (two layer response), it may be a result of many different dynamical normal modes. Figure 11(d) shows the vertical distribution of the eigenvector of EOF 2. Figures 11(b) and 11(d) indicate that mode 2 is prominent at 50 m (Fig. 10).

The amplitude of the baroclinic pressure gradient rapidly decreases as the mode number increases. Figure 12 shows time series of acceleration, baroclinic pressure gradient, stress function and friction at the surface as described by (4) for dynamical normal modes 1 through 4. This figure shows that mode 2 modal current is as strong as mode 1 modal current. For the standard value of K, only the mode 1 baroclinic pressure gradient has comparable amplitude to other terms in (4). (This term is omitted in the figure of modes 3 and 4 of Fig. 12 since they are very small and are not separable from the line at 0 with the scale used here.) This appears to be a result of combined effects of weaker excitation of baroclinic pressure gradient and stronger dumping when mode number is high. The significance of the baroclinic pressure gradient is affected by forcing frequency and eddy viscosity. The amplitude of the baroclinic pressure gradient increases as forcing frequency decreases. When K in (14) is large, the differences of effective friction coefficients between different modes increase, and therefore, the baroclinic pressure gradients at higher modes are more suppressed relative to lower modes. The larger eddy viscosity causes more suppression of the high-frequency component of baroclinic pressure gradient.

At shallow depths the relative importance of the

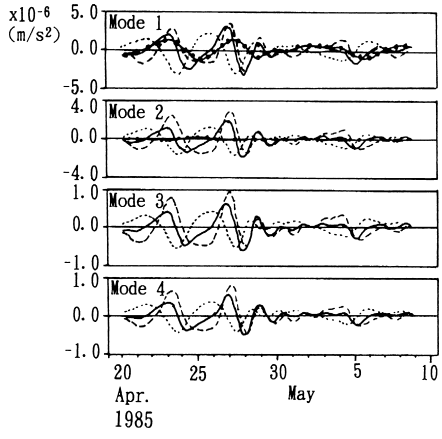

Fig. 12. Time series of acceleration ($\partial u/\partial t$, —), baroclinic pressure gradient ($C^2\partial\zeta/\partial x$, -•-•-), stress function (ϕ, – –) and friction ($-ru$, - - -) of modes 1 through 4 at the surface. The baroclinic pressure gradients of modes 3 and 4 are omitted since they were very small with the scale used here.

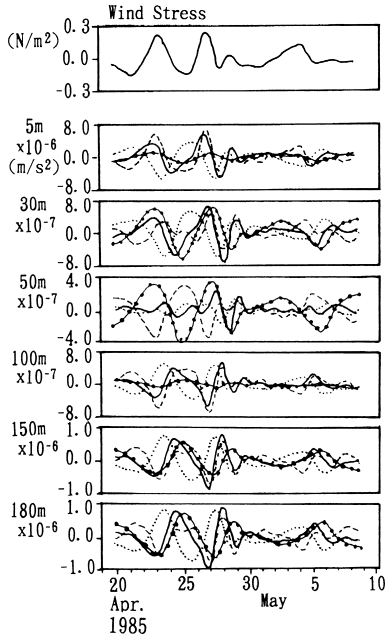

Fig. 13. Time series of acceleration ($\partial u/\partial t$, —), baroclinic pressure gradient ($C^2\partial\zeta/\partial x$, -•-•-), stress function (ϕ, – –), and friction ($-ru$, - - -) summed over 15 mode at several depths. Top panel shows wind stress.

baroclinic pressure gradient is small due to the large amplitude of the stress function and the friction. The vertical distribution of the amplitudes of this term summed over all the modes follows closely the vertical distribution of dQ/dz of mode 1 because of the small amplitudes of higher modes (Fig. 12). At depths close to the bottom, the baroclinic pressure gradient becomes more important due to the smaller amplitudes of the stress function and the friction. Lower panels of Fig. 13 show the time series of the acceleration, the baroclinic pressure gradient, the stress function, and the friction summed over 15 modes at several depths. This figure illustrates the above descriptions. The top panel of Fig. 13 shows the time series of wind stress and this figure indicates that the observed reduction of the amplitude and eventual reversal of the sign of acceleration while wind was blowing in the same direction is due to the friction.

6. Conclusion

Currents from the surface to about 10 m are strongly affected by wind in Puget Sound. The wind effects on currents at depths between 20–30 m are strongly affected by the near-surface stratification. When stratification is weak, currents at these depths are strongly affected by wind. When stratification is strong, the depth limit where wind can directly affect the current is about 30 m. In Puget Sound, strong stratification tends to occur between 10–30 m due to the advection of fresher water or to the large precipitation. The wind effects on currents at about 100 m and below are statistically significant and have opposite directions to the near surface responses. The wind effects between about 30–100 m have mixed between the responses at near-surface depths and at depths greater than 100 m. The EOF analysis applied to the band-pass filtered 1985 velocities shows that mode 1 contains 69% of total variance and is highly correlated to the wind speed and, thus, the wind has the strongest effect on sub-tidal currents. The results of EOF analysis applied to 1984 and 1985 data, excluding all of near surface data, suggest that this holds not only for the surface current but also for the current at mid-depths of about 100 m. Although observed wind induced currents both at the surface and at mid-depths lag the wind, acceleration indicates that the responses of currents to wind events are almost instantaneous. This suggests that the time lag between wind and current is simply caused by the fact that the currents lag behind the accelerations. When stratification is weak, direct responses to the wind events can propagate to about 100 m, and there is no consistent depth where one can separate upper and lower layers. The time series of the acceleration during wind events show that the acceleration may reach a maximum and then start decreasing and eventually change sign before the wind changes its direction. Approximate estimates suggest that friction at solid boundaries is likely the major cause of these phenomena. The continuously stratified model results agree with this conclusion.

Acknowledgements

The authors thank Dr. Rattray at University of Washington, Dr. Inaba at Tokai University, Dr. Sugimoto at University of Tokyo, the reviewers and others at PMEL, UW and elsewhere for their various support and, especially, their very constructive comments and critiques.

Appendix. Inter-Modal Differences of Model Currents

The correlations between the currents of the different dynamical normal modes are very high (thus EOF can not separate dynamical normal modes) but they are not identical. The differences between different dynamical normal modes of current originate from three sources; change of the time scale of the integrand in the solution (15) (low-pass filtering effect), the phase lag due to the difference of the effective friction coefficients, and the baroclinic pressure gradient which is only significant for lower modes. The first two are the differences due to the stress functions of the different dynamical normal modes.

Equation (15) shows that the time integration with exponential function acts as a low-pass filter, and the sharpness of that filter is controlled by the effective friction coefficient α_n which acts as a weighting function. This low-pass filter effect becomes less sharp as α_n increases either due to an increase of eddy viscosity or mode number. Note that this result does not mean that the high frequency forcing

excites higher modal currents effectively compared to the lower frequency forcing. The physical explanation is that low frequency forcing penetrates into the water column deeper than the high frequency forcing, and the depths of the first zero crossing of dQ/dz of the lower modes are deeper than the higher modes (Fig. 9(b)). To explain this simply, we assume the forcing is sinusoidal, ignore the pressure gradient, and assume the eddy viscosity K_z is constant. With these conditions, stratification is ignored. In this case, the boundary value problem becomes an oscillatory Couette flow, and the solution with the surface stress $Te^{i\omega t}$, where T is a constant, $i^2 = -1$ and ω is a forcing frequency, has a form of

$$u = \mathrm{Re}\left\{\frac{T(1-i)}{\sqrt{2K_z\omega}}\exp\left(-\sqrt{\frac{\omega}{2K_z}}z\right)\exp\left[i\left(\omega t+\sqrt{\frac{\omega}{2K_z}}z\right)\right]\right\}, \tag{A1}$$

$$\frac{\partial\mu}{\partial z} = \rho\,\mathrm{Re}\left\{\sqrt{\frac{\omega}{2K_z}}T(1+i)\exp\left(-\sqrt{\frac{\omega}{2K_z}}z\right)\times\exp\left[i\left(\omega t+\sqrt{\frac{\omega}{2K_z}}z\right)\right]\right\}.$$

This solution shows the vertical gradient of stress decays exponentially as depth increases, and it will decay faster as frequency increases. The effect of change of the eddy viscosity is inverse to the change of the forcing frequency. As the depth of influence decreases, it is expected from (6) and Fig. 9(b) that the inter-modal difference of part of the stress function directly caused by wind forcing decreases because the numerator of stress function is a convolution integral of the vertical gradient of stress at a given time with dQ_n/dz. Thus, because of the changes of sign of dQ/dZ at shallower depths, higher modes are excited less effectively at wide frequency range, and low frequency forcing can excite lower modes more effectively. Note that the assumption of well mixed surface layer adopted in some other models (Proehl and Rattray, 1984; Shay *et al*., 1989) is equivalent to that dQ_n/dz is constant in Z in the surface mixed layer and thus there is no inter-modal difference of the stress function in the surface mixing layer.

As the mode number increases, the baroclinic pressure gradient term becomes small (Fig. 12), and at certain mode numbers, this term can be negligible in (15). In that case, the solution is approximated by

$$u_n \cong \int_0^t T_n(\sigma)e^{-\alpha_n(t-\sigma)}d\sigma. \tag{A2}$$

As the mode number further increases, α_n becomes large, and at a certain point, the time scale of the exponential function becomes so small that the solution is approximated by

$$u_n \cong \frac{Ts(t)}{\alpha_n}\left(1-e^{-\alpha_n t}\right)\Big/\int_{-H}^{0}\rho\left(\frac{dQ_n}{dz}\right)^2 dz. \tag{A3}$$

This solution shows that higher modes of model velocities are identical except for the amplitude after the decay of the effect of the initial condition. The amplitude of modal current decreases as mode number increases because of the increase of internal stress due to the increase of vertical shear. In (A3), u_n decreases due to the increases of α_n in the denominator. The vertical integration in the denominator does not change appreciably. With the rigid rid condition with constant N, this integration becomes constant, H/2. It must be noted that the pressure gradient should be retained near the boundary, where the wind stress and the pressure gradient balance each other to satisfy the boundary condition. Approximate e-folding scale of this boundary effects is $2C_n/\alpha_n$ from (16).

Figure A1 shows amplitudes of the lowest three dynamical normal modal currents as a function of forcing frequency at the first maximum after sinusoidal forcing is turned on (Fig. 7, MA). The first maximum is chosen because real wind forcing is quite unlikely to be purely sinusoidal. Here the values correspond to those at the surface. The baroclinic pressure gradient does not have any effect when the forcing frequency is high because effects of it do not arrive before the time of first maximum as shown by (16). These frequency limits are shown as short vertical lines on the figure. This figure shows that the amplitude of lower dynamical normal modes decreases both at the low and high frequency ranges. The decrease at the low frequency range is caused by the effects of baroclinic pressure gradient. Without the baroclinic pressure gradient, the amplitude of a model velocity asymptotically approaches a constant as the forcing frequency decreases.

The phase lag between currents of different normal

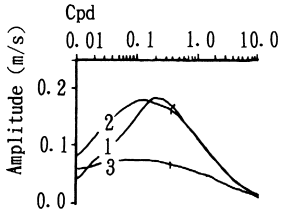

Fig. A1. Amplitude of the lowest three modal currents as a function of forcing frequency at the first maximum after sinusoidal forcing was turned on. The numbers in this figure are the mode numbers and the short vertical lines on each plot show the frequency limit where baroclinic pressure gradient has no effect.

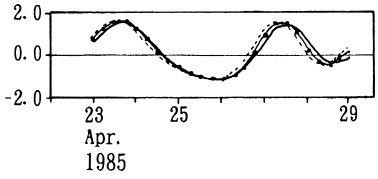

Fig. A2. Time series of modal velocities of mode 1 (—), mode 2 (-•-•-) and mode 10 (- - -). Arbitrary constants are multiplied to these time series to make comparison easier.

modes can be explained by ignoring pressure gradient term in (15) at first which is valid for higher modes and/or high frequency forcing. If forcing is sinusoidal as $Ts = T \sin\omega t$ where T is a constant, with the initial condition $u = 0$ at $t = 0$, the phase lag θ is, using the relation in MA ((8), MA),

$$\theta = \sin^{-1}\left(\frac{\omega}{\sqrt{\alpha_n^2 + \omega^2}}\right).$$

As α_n increases, this phase lag approaches zero. Figure A2 shows time series of model velocities of dynamical normal modes 1, 2 and 10 to show this phase lag. Here, mode 10 was selected as an example of high-mode velocity (A3). Mode 15, the highest mode computed, was practically identical to mode 10 except its amplitude, and visual separation is not possible for the scale of time-axis used in Fig. A2. The amplitudes of these time series are adjusted by multiplying arbitrary constants to make comparison easier. The frequency of the event shown in Fig. 9 is about 1.8×10^{-5} rad/s (period is about 4 days) and the phase lag between mode 1 and 2 corresponds to about 2.4 hours from above relation. This phase lag roughly match the phase lag appeared in Fig. A2. The phase lag due to the baroclinic pressure gradient is determined by C_n and the distance between the boundary and the position x from (16). This time lag between mode 1 and 2 is about 17 hours but the amplitude of baroclinic pressure gradient of mode 2 is very small and it is not apparent in Fig. A2.

References

Bretschneider, D. E., G. A. Cannon, J. R. Holbrook and D. J. Pashinski (1985): Variability of subtidal current structure in a fjord estuary: Puget Sound, Washington. *J. Geophys. Res.*, **90**, 11949–11958.

Buckley, J. R. and S. Pond (1976): Wind and the surface circulation of a fjord. *J. Fish. Res. Board. Can.*, **33**, 2265–2271.

Cannon, G. A. (1983): An overview of circulation in the Puget Sound estuarine system. *NOAA Tech. Memo.*, ERL PMEL-48, 30 pp.

Cannon, G. A., J. R. Holbrook and D. J. Pashinski (1990): Variations in the onset of bottom-water intrusions over the entrance sill of a fjord. *Estuaries*, **13**(1), 31–42.

Cokelet, E. D. (1992): Axial and cross-axial winter winds over Puget Sound. *Mont. Wea. Rev.*, **120**, 826–834.

Csanady, G. T. (1972): Response of large stratified lakes to wind. *J. Phys. Oceanogr.*, **2**, 3–13.

Davis, R. E. (1976): Predictability of sea surface temperature and sea level pressure anomalies over the North Pacific Ocean. *J. Phys. Oceanogr.*, **6**, 249–266.

Farmer, D. M. (1976): The influence of wind on the surface layers of a stratified inlet: Part II. Analysis. *J. Phys. Oceanogr.*, **6**, 941–952.

Farmer, D. M. and T. R. Osborn (1976): The influence of wind on the surface layers of a stratified inlet: Part I. Observations. *J. Phys. Oceanogr.*, **6**, 931–940.

Fjeldstad, J. E. (1963): Internal waves of tidal origin. *Geofys. Publr.*, **25**, 1–73.

Friebertshauser, M. A. and A. C. Duxbury (1972): A water budget study of Puget Sound and its subregions. *Limnol. Oceanogr.*, **17**, 237–247.

Gill, A. E. (1982): *Atmosphere-Ocean Dynamics*. Academic Press, London, 662 pp.

Hansen, D. V. and M. Rattray, Jr. (1965): Gravitational circulation in straits and estuaries. *J. Mar. Res.*, **23**(2), 105–121.

Large, W. S. and S. Pond (1981): Open ocean momentum flux measurements in moderate to strong winds. *J. Phys. Oceanogr.*, **11**, 324–336.

Lavelle, J. W., E. D. Cokelet and G. A. Cannon (1991): A model study of density intrusions into and circulation within a deep, silled estuary: Puget Sound. *J. Geophys. Res.*, **96**, 16779–16800.

Matsuura, H. (1995): An application of a two-layer model to wind driven sub-tidal currents in Puget Sound. *J. Oceanogr.*, **51**, 571–584.

McCreary, J. P. (1981): A linear stratified model of the coastal undercurrent. *Philos. Trans. Roy. Soc. London*, **A302**, 385–413.

North, G. R., T. L. Bell and R. F. Cahalan (1982): Sampling errors in the estimation of empirical orthogonal functions. *Mon. Wea. Rev.*, **110**, 699–706.

Pashinski, D. J. (1985): Comparison of current meters in a tidaly dominated flow. *Ocean 85 Proceedings: Ocean Engineering and the Environment*, **2**, 738–741.

Pickard, G. L. and K. Rodgers (1959): Current measurements in Knight Inlet, British Columbia. *J. Fish. Res. Bd. Canada*, **16**(5), 635–678.

Preisendorfer, R. W., F. W. Zwiers and T. P. Barnett (1981): Foundations of principal component selection rules. *SIO Ref. Series*, **#81-4**, 192 pp.

Pritchard, D. W. and E. C. Vieira (1984): Vertical variations in residual current response to meteorological forcing in the Mid-Chesapeake Bay. p. 27–65. In *The Estuary as a Filter*, Academic Press.

Proehl, J. A. and M. Rattray, Jr. (1984): Low-frequency response of wide-deep estuaries to non-local atmospheric forcing. *J. Phys. Oceanogr.*, **14**, 904–921.

Shay, L. K., R. L. Elsberry and P. G. Black (1989): Vertical structure of the ocean current response to a hurricane. *J. Phys. Oceanogr.*, **19**, 649–669.

Svendsen, H. and R. O. R. Y. Thompson (1978): Wind-driven circulation in a fjord. *J. Phys. Oceanogr.*, **8**, 703–712.

Winter, D. F. (1973): A similarity solution for steady-state gravitational circulation in fjords. *Est. Coastal Mar. Sci.*, **1**, 387–400.